Effect of the porosity and microstructure on the mechanical properties of organic xerogels

S.L. Flores-López[1], B. Karakashov[2], L.A. Ramírez-Montoya[1], J.A. Menéndez[1], V. Fierro[2], A. Arenillas[1], M.A. Montes-Morán[1, *], A. Celzard[2]

[1]Instituto de Ciencia y Tecnología del Carbono, INCAR-CSIC, Francisco Pintado Fe, 26, 33011, Oviedo, Spain

[2]Institut Jean Lamour, UMR CNRS-Université de Lorraine nº7198, ENSTIB, 27 rue Philippe Séguin, BP 21042, 88051 Epinal cedex 9, France

Abstract

The synthesis of resorcinol-formaldehyde (RF) xerogels is versatile enough to provide materials with custom pore size distributions in the meso/macroporous range. Specifically, seven xerogels were synthesised by changing the pH of the same RF solution, from pH 3 to pH 6. The resulting materials presented meso/macropore size distributions with average pore sizes from <5 to 510 nm, as determined by Hg intrusion and N_2 adsorption. Most of the RF xerogels had very similar geometric densities, except for the gels obtained at the two highest pH values, which were more dense. Both flexural and uniaxial compression tests were carried out to determine the dependence of strength and stiffness on the porosity of the xerogels. The results followed a power-law relationship between the mechanical properties and the density of the materials. However, two series of RF xerogels were found to fit such law independently, with the gels obtained at the three most acidic pH values (pH 3-4) showing unexpectedly high compression moduli. Further characterisation of the xerogels microstructure revealed the existence of rod-like microstructures that would bear most loads during the compression tests. These microstructures would act as struts that, once broken, would cause the catastrophic failure (bursting) of the xerogel.

Keywords: RF xerogel; mechanical properties; microstructure; porosity

1. Introduction

Since the first synthesis of resorcinol-formaldehyde (RF) gels reported by Pekala in 1989 [1], these materials have received increasing attention due to their potential application in different fields, mainly as adsorbents in fluid media, catalysts supports, energy absorbers, energy storage and electrochemistry [2–4]. This is a consequence of the tight control on the porosity and surface chemistry of these materials, one of their main advantages. Thus, pore size distributions and/or pore volumes can be tuned by the adjustment of several physical and chemical variables during RF polymerisation, curing and drying steps. The main parameters that affect the porosity of these RF polymers are the temperature and duration of the reactions, the amount of reactants and ratios, and particularly the concentration and type of pH regulator of the precursor solution [2,3,5–7].

Furthermore, the possibility of synthesising RF gels in a monolithic form further broadens the variety of potential applications of these materials, for example as stationary phases in separation technologies. When using monoliths, their mechanical properties become a fundamental issue [3,5]. The dependence of the mechanical properties of monoliths on their microstructure has been studied extensively for materials such as foams, carbons and silica aerogels, suggesting that there is an universal correlation based on the chemical structure of each type of material [3,4,6,8–12]. This dependence is usually represented by a mathematical correlation (power law) between mechanical parameters such as modulus and strength, and the densities of the studied materials [9,13–17]. Based on the open/closed-cell theory, the exponent values of such power law have been related to the connectivity of the materials. Thus, exponents between 2 and 3 are expected for foam-like structures, whereas exponents >3 are linked to irregular or fractal structures [18,19].

So far, studies on the mechanical properties of monolithic RF gels have focused on the effect of the amount of basic catalysts used for the synthesis of low-density gels, starting mainly from pH values around 5 [5,19]. However, little work has been done on the subject of RF gels synthesised under acidic conditions, which is certainly of interest given the great versatility of these materials. In that sense, it would be very relevant for certain applications if the mechanical properties of RF monoliths prepared over a wide range of pH could also be controlled during the polymerisation reactions.

Therefore, the aim of this work is to expand the understanding of the effect of the porosity and microstructure of RF xerogels on their mechanical properties. To achieve this goal, a series of RF monoliths were prepared from precursor solutions covering a wide pH range (i.e., pH 3 to 6). The monoliths were mechanically tested in flexion and compression, and the corresponding moduli and strengths were fitted to a power law of materials densities.

2. Experimental

2.1 Synthesis of materials

Organic xerogels in monolithic form were synthesised by polycondensation of resorcinol (R, 99%, from Indspec) and formaldehyde (F, 37 wt.% in water, 10% methanol content, from Merck), using deionised water as solvent. The quantities of each reactant were fixed to obtain a molar ratio R/F and a dilution ratio D (molar ratio between solvent and reactants) of 0.5 and 5.6, respectively. From this homogeneous mixture, seven different precursor solutions of pH 3-6 every 0.5 pH units were prepared by addition of NaOH. Amounts of these precursor solutions were carefully poured into glass pipettes (5.5 mm in diameter and 100 mm in length). After 48 h at 85°C in this open system, dried monoliths were extracted from the glass pipettes, and each sample

was carefully cut into perfect cylindrical shapes. The length of the cylinders depended on the requirements of each analysis (see below). Throughout this work, samples are referred to as OX, which stands for organic xerogel, followed by the pH value of the precursor solution.

2.2 Characterisation of the monoliths

Elemental analysis (i.e., C, H, N, S and O wt.%) of the OXs were carried out in LECO-CHNS-932 and LECO-TF-900 microanalysers [13,20].

The textural characterisation of the monoliths included the measurement of their density, porosity and morphology. Prior to each measurement, the samples were outgassed at 60ºC overnight.

The geometric density (ρ_{geo}) was evaluated by weighing cylinders of known dimensions, the helium density (ρ_{He}) was determined by helium pycnometry (AccuPyc 1330 from Micromeritics), and the bulk density (ρ_{Hg}) was determined by mercury porosimetry (AutoPore IV porosimeter from Micromeritics). The porosity (P, %) was calculated from the geometric and helium densities according to the expression:

$$P = (1 - \frac{\rho_{geo}}{\rho_{He}}) \times 100 \quad (1)$$

Mercury porosimetry was also used to obtain pore size distributions and pore volumes from the intrusion curves. The porosity of the monoliths was further characterised using N_2 adsorption-desorption isotherms at -196ºC (Tristar II from Micromeritics). The BET surface areas (A_{BET}) and N_2 pore volumes were calculated from these isotherms.

The morphology (microstructure) of the xerogel monoliths before and after the compression tests was examined using a scanning electron microscope (SEM, Quanta FEG 650) with an accelerating voltage of 20 kV and a secondary electron detector

(EDT, Everhart-Thornley). All samples were metallised with iridium and attached to an aluminium tap using double-sided conductive adhesive tape.

The mechanical characterisation was carried out in a controlled environment (20°C average temperature and 50-60% relative humidity), using an INSTRON 5944 universal testing machine equipped with a 2 kN head, set and controlled with the BLUEHILL software.

The compression tests were performed on cylindrical monoliths with length to diameter ratios always lower than 1 (i.e., lengths < 5.5 mm), in order to avoid possible bending deformation that would lead to measurement errors. Uniaxial compression tests were performed in the longitudinal direction of the material (see Figure S1 for details). The full compression characteristics were recorded using the compression set (i.e., parallel platens with patella) and a head displacement rate of 0.2 mm min^{-1} [10,21]. A maximum load of 1.6 kN was set to protect the testing machine. The stress-strain (σ_{com}-ε_{com}) curves recorded in the INSTRON machine are based on equations (2) and (3), from values of force (F_z), displacement (change per unit length of thickness, δ_c) and sample dimensions (radius R_d, cross-section S, and length L_0):

$$\sigma_{com} = \frac{F_z}{S} = \frac{F_z}{\pi {R_d}^2} \quad (2)$$

$$\varepsilon_{com} = \frac{\delta_c}{L_0} \quad (3)$$

These data were used to determine the yield strength (σ_{yi}) of the analysed materials, as well as to obtain the Young's modulus (E_{com}), according to:

$$E_{com} = \sigma_{com}/\varepsilon_{com} \quad (4)$$

The Young's modulus was calculated as the slope of the linear part of the stress-strain curve, and the compressive (yield) strength as the stress value for the elastic limit of the

material, defined as the maximum stress applied before reaching permanent deformation.

The flexural tests were performed using a three-point bending configuration with cylindrical specimens of length equal to 10 D_i, where D_i corresponds to the diameter of the sample. The measurements were carried out in the same device used for the compression tests, but in this case with two anvil supports on the base and a single bending fixture on the upper force sensor (see also Figure S1). The support beam is graduated lengthwise in metric units for accurate positioning of the anvils. The anvils must be spaced 8 D_i apart and equidistant from the midline. To set the initial displacement position before the beginning of each experiment, the upper fixture was moved downward until full contact with the material was established at a predefined force of 0.1 N. Then, a head displacement rate of 0.2 mm min^{-1} was used for performing the measurements [22–27].

From the recorded data (i.e., force and displacement at the midpoint), the stress-strain curve can be calculated, and thus the elastic modulus and flexural strength. The flexural stress for a bending rod of circular cross-section is given by the following equation:

$$\sigma_{flex} = M\,c\,/\,I \tag{5}$$

where σ_{flex} is the stress, M the applied moment, c the distance of the outer surface from the neutral axis, and I the moment of inertia of the cross-section. For a circular cross-section, and considering that the material deformation follows Hooke's law:

$$I = \frac{\pi\, {D_i}^4}{64} \tag{6}$$

$$c = R_d = \frac{D^i}{2} \tag{7}$$

$$M = \frac{F_z a}{2} \quad (8)$$

where a is the moment arm. The moment arm is $L_0/2$ in the three-point loading configuration. Hence, the flexural stress becomes:

$$\sigma_{flex} = \frac{F_z L_0}{\pi R_d^3} \quad (9)$$

According to the simple beam theory of Euler-Bernoulli, concerning small deflection and small changes in elements length after bending (which is the case of the materials analysed in this work), the flexural modulus (E_{flex}) is given by the slope of the force-deflection (δ) curve as expressed by equation (10). The latter can be combined with Hooke's law in order to express the strain ε_{flex} of the material using the displacement in midpoint deflection (δ_f):

$$E_{flex} = \frac{F^z}{\delta} \frac{{L_0}^3}{12\pi {R_d}^4} = \frac{\sigma_{flex}}{\varepsilon_{flex}} \quad (10)$$

$$\varepsilon_{flex} = \frac{6\delta_f D_i}{{L_0}^2} \quad (11)$$

From stress-strain curves, the flexural strength can also be obtained within the elastic limit of each material.

3. Results and discussion

The materials obtained from solutions with different pH values were first characterised from a structural point of view. It is worth mentioning that, although all the monoliths were synthesised using pipettes with virtually the same dimensions as described in the experimental section, the rods obtained from different precursor solutions showed variations in diameter. Indeed, this value was 5.4 ± 0.15 mm for monoliths OX3 to OX5, 5 ± 0.03 mm for OX5.5, and 4.45 ± 0.05 mm for OX6. From the measurements of

dimensions and masses of the monoliths prepared for this analysis, ρ_{geo} of the materials was calculated. Figure 1 shows its variations, as well as those of the other measured densities (i.e., geometric, He and Hg densities), with the pH of the precursor solution. The differences between ρ_{geo} and ρ_{Hg} are negligible for all materials. They are nearly constant (0.30-0.35 g/cm^3) for samples obtained at a pH between 3 and 5, and increase for OX5.5 and OX6. This remarkable densification of materials obtained from solutions of higher pH should be related to the aforementioned radial shrinkage of the monoliths. On the other hand, ρ_{He} remains constant (ca. 1.4 g/cm^3) for all samples. This was an expected outcome because the same R/F ratio was used for the synthesis of all the OXs under study (see Section 2). This same ratio produced materials with identical composition (Table S1), which in the end determines the results of He density.

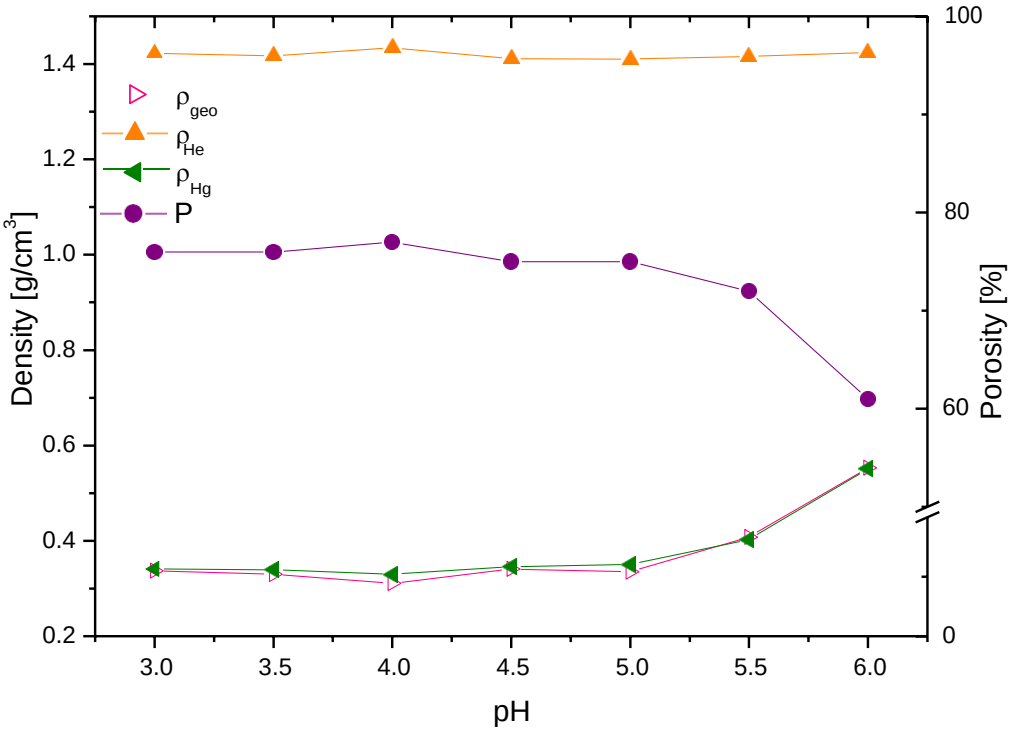

Figure 1. Relationship between different densities and porosities of the RF xerogels studied and the pH of their precursor solutions.

Figure 2 shows the N_2 adsorption-desorption isotherms of the OXs. The shape of the isotherms was affected by the pH of the precursor solution. Thus, the samples OX3 and

OX3.5 gave type III isotherms, according to the IUPAC classification [14], characteristic of macroporous samples with hardly identifiable monolayer formation during N_2 adsorption. The samples obtained at pH 4 to 5 showed type II isotherms, indicating that they are macroporous materials with unrestricted monolayer-multilayer adsorption up to high relative pressure p/p^0. The adsorption of N_2 on these samples at both low and high relative pressures increased with the pH of the precursor solution due to their relatively higher microporosity and the appearance of narrower pores detected by this technique. Finally, OX6 presented a type IV isotherm with a hysteresis loop due to capillary condensation, indicating the presence of narrow mesopores. The isotherm of OX5.5 might also be type IV, with a hysteresis loop much narrower than that of OX6.

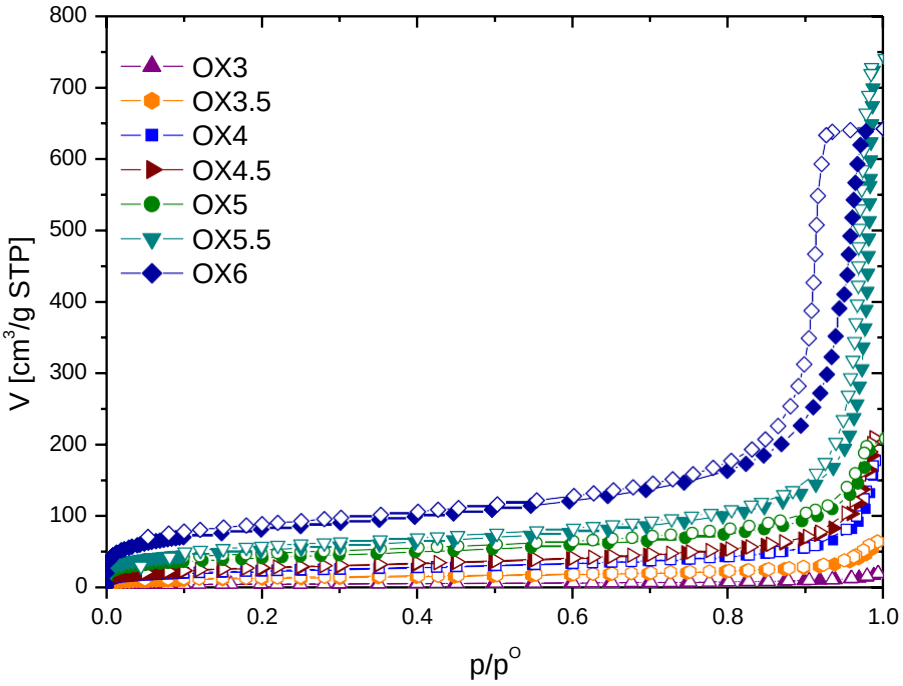

Figure 2. N_2 adsorption-desorption isotherms of the studied RF xerogels.

The textural parameters calculated from these nitrogen adsorption isotherms are collected in Table 1. The variations in the values of V_{total} and A_{BET} in the sample series confirm the formation of narrower pores as the pH of the OX precursor solution

increases. In addition, the decrease of V_{total} observed for OX 6 could be attributed to the collapse that occurred during the aforementioned densification (Figure 1). The influence of pore size on the material densification has been previously studied [6,15,16].

Table 1. Textural properties of the organic xerogel monoliths.

Sample	Pore volume					Pore size			A_{BET}
						L_t[c]	L_{Hg}[a]	L_{N2}[e]	
	cm^3/g	cm^3/g	cm^3/g	cm^3/g	cm^3/g	nm	nm	nm	m^2/g
OX3	1.966	0	1.966	0.031	0.030	510	510	ND*	15
OX3.5	2.055	0	2.055	0.100	0.095	276	276	ND*	43
OX4	2.198	1.379	0.819	0.275	0.269	73	101	ND*	73
OX4.5	2.015	1.503	0.512	0.323	0.317	39	61	ND*	88
OX5	1.887	1.447	0.440	0.310	0.296	33	53	ND*	140
OX5.5	1.592	1.459	0.133	1.124	1.109	8	18	17	176
OX6	0.838	0.838	ND*	0.989	0.966	ND*	ND*	5	266

[a] True Hg pore volume = [intruded volume (V_p)] – [volume attributed to squeezing (V_t)]
[b] Pore volumes obtained from N_2 isotherms
[c] Pore size measured by Hg porosimetry
[d] True pore size calculated from Hg porosimetry following the equations of Job et. al. [8]
[e] Pore size calculated from N_2 isotherms using the NLDFT model (Figure S2)
ND* Non-determined

In order to characterise the meso-/macro-pores of the OXs materials, mercury porosimetry is preferable due to the inherent limitations of N_2 adsorption at -196ºC. Figure 3 shows the obtained Hg intrusion profiles. Three types of intrusion curves are clearly observed. The samples OX3 and OX3.5 display curves corresponding to a unique process of Hg intrusion into the pores. The intrusion curves of samples OX4, OX4.5 and OX5 show a gradual slope of intruded volume and then a sudden intrusion at medium pressures. Finally, the Hg intrusion in samples OX5.5 and OX6 is relatively steady from low to high pressures, with no sharp sudden step. It should be emphasised here that different phenomena may occur during Hg intrusion into the pore network of xerogels, giving rise to the differences observed in the intrusion curves described above. Thus, phenomena such as sample squeezing, crack generation and Hg penetration

between sample particles are to be expected. These processes are not always correctly identified and taken into account when interpreting Hg intrusion data. It is important here to identify the pressures at which real intrusion phenomena occur (P_t), which correspond to 2.2, 4.5, 17.5, 34.7 and 39.8 MPa for samples OX 3, 3.5, 4, 4.5 and 5, respectively.

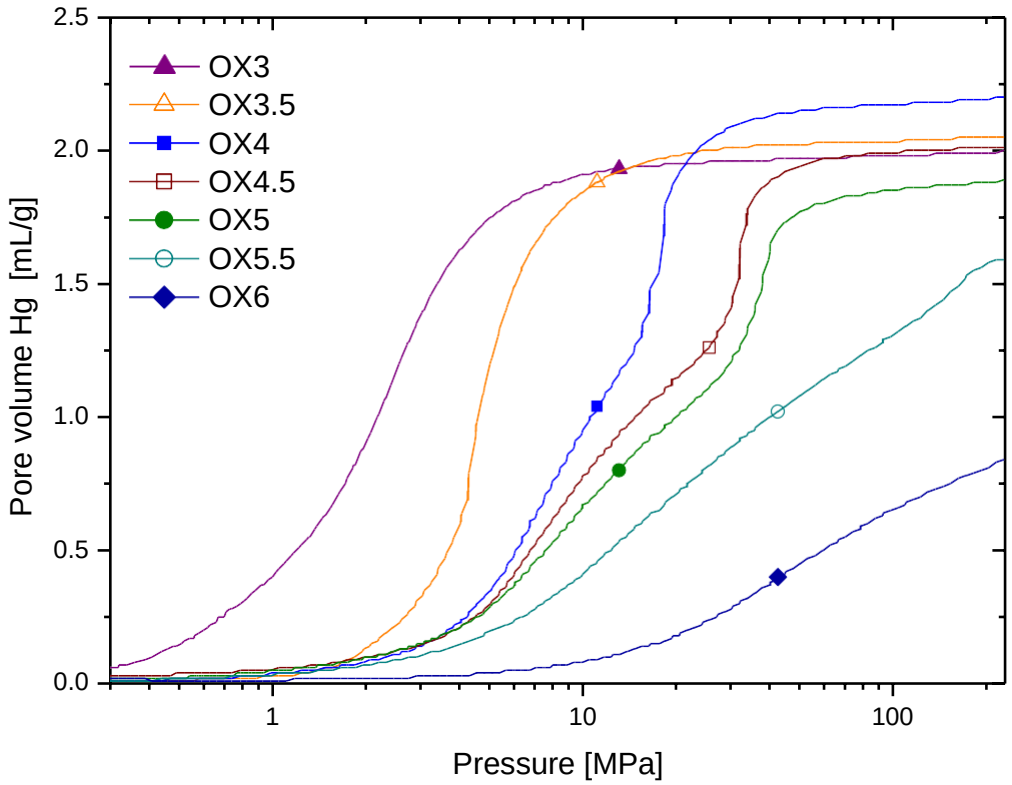

Figure 3. Volume of Hg intruded as a function of pressure for the studied RF xerogels.

These mentioned effects become possibly more evident when analysing the pore size distributions of the materials derived from the porograms (Figure 4). OXs 4-5.5 have a composite profile, with a relatively narrow band at lower pore sizes and a much wider and less intense band at higher pore sizes. In the case of OX6, the narrow band is absent and the pore size distribution has a continuous profile spanning from 1000 to 5 nm. This suggests that the porosity of this particular material cannot be reliably characterised by Hg intrusion.

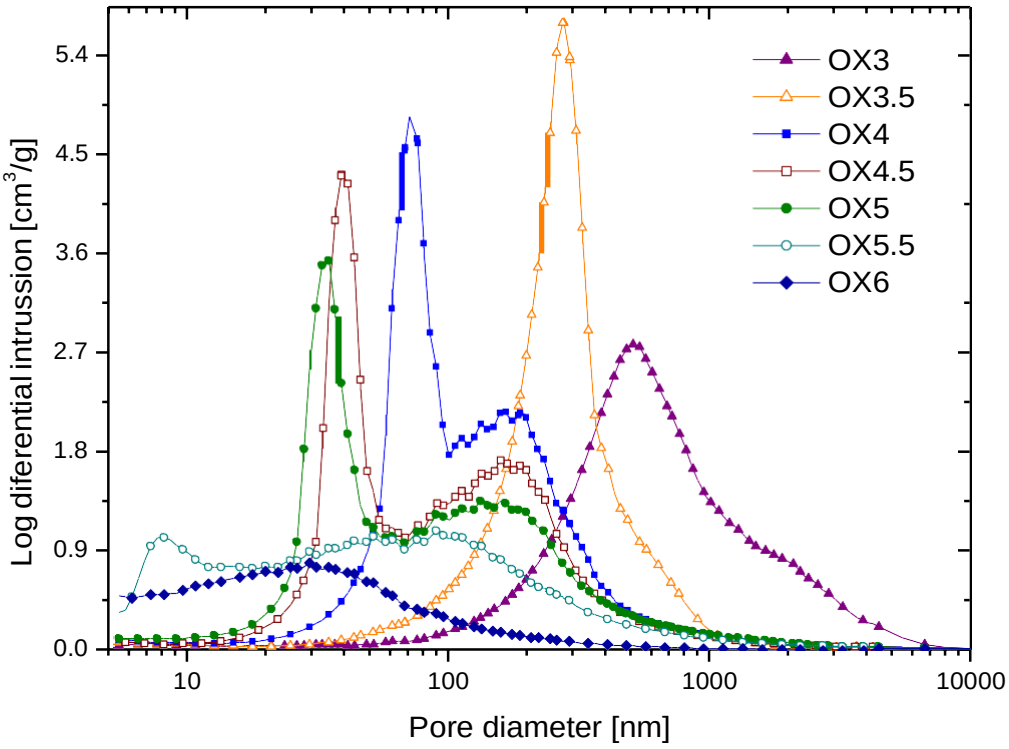

Figure 4. Pore size distributions of xerogel RF samples as determined by Hg intrusion.

The wide bands of the pore size distributions are a consequence of the compression of the OXs materials under Hg intrusion. According to Job et al. [8], the squeezing of samples biases the assessment of pore size and pore volume for this type of material. Thus, the initial collapse of the pores reduces their diameter and the characteristic (narrower) pore band is shifted to the left from its initial value. In addition, the volume of intruded Hg is affected by the volume generated during the squeezing of the samples. Moreover, the original pore size (L_{Hg}) and intruded volume (V_{Hg}) can be calculated from the size of the compressed pores (L_t) using the equations proposed by Job et al. [8] (Eq. 12 and 13), where V_p is the (conventional) pore volume measured by mercury porosimetry and V_t is the pore volume measured at the pressure at which intrusion begins (P_t).

$$V_{Hg} = V_p - V_t \tag{12}$$

$$L_{Hg} = L_t \left(\frac{V_p}{V_{Hg}}\right)^{1/3} \quad (13)$$

Table 1 also summarises the corrected values of pore volume and pore size determined by Hg porosimetry. These results show a clear difference in pore size of the OXs samples, ranging from narrow mesopores (Hg porosimetry is able to characterise pores ≥3.7 nm) to pore sizes larger than 1000 nm. In contrast to the total pore volume obtained from N_2 isotherms, the lower the pH of the precursor solution, the higher the pore volume measured by Hg intrusion. This shows the relevance of both techniques for characterising the textural properties of the OXs materials, N_2 adsorption-desorption isotherms being the way of characterising narrow pores (i.e., microporosity and narrow mesoporosity) while Hg porosimetry can only characterise wider pores (i.e., wide mesoporosity and macroporosity). Therefore, a low pH in the precursor solution leads to RF xerogels having low microporosity but high macroporosity, while a pH of 6 results in RF xerogels having virtually no wide pores (i.e., it cannot be characterised by Hg porosimetry) and higher microporosity (see Figure S2), which implies achieving a wide range of porosity from the pH adjustment of the precursor solutions.

The stress-strain curves corresponding to the flexural and compressive tests of the OXs are shown in Figure 5. The actual (i.e., not average) sample diameters were used for the stress calculation in both mechanical tests. The diameter of the OX rods tested in flexion was measured at three different points. Although small differences were observed within the replicates, the variation in diameter along a given rod was less than 0.5% of the actual diameter considered.

In the case of the flexural tests (Figure 5a), linear deformation behaviour followed by abrupt failure was observed for all OXs samples, as already reported elsewhere [3,17,28], i.e., all behaved as brittle materials. Hence, flexural moduli and flexural

strengths were calculated from the stress-strain curves and the results are presented in Table 2. The lowest flexural moduli were observed for the OX samples obtained at intermediate pH (OX4 - OX5). Thus, a substantial increase in materials stiffness for OX6 resulted in a flexural modulus four times higher than that of OX4 - OX5.

Failure under compression was more complex and was found to depend on each particular OX sample (Figure 5b). A common feature of all the tests was the existence of an initial curvature in the very low strain regime of the stress-strain curves that was ascribed to the so-called “parallelism rectification” (Figure S3) [5,10]. Thus, the initial linear deformation was considered the onset of the real compression of the material. In general, compression cracks were concentrated or propagated in the same direction as uniaxial compression, along the length of the monoliths. Consequently, small fragments were ejected from the outside diameter to different extents during the tests (Figure 6).

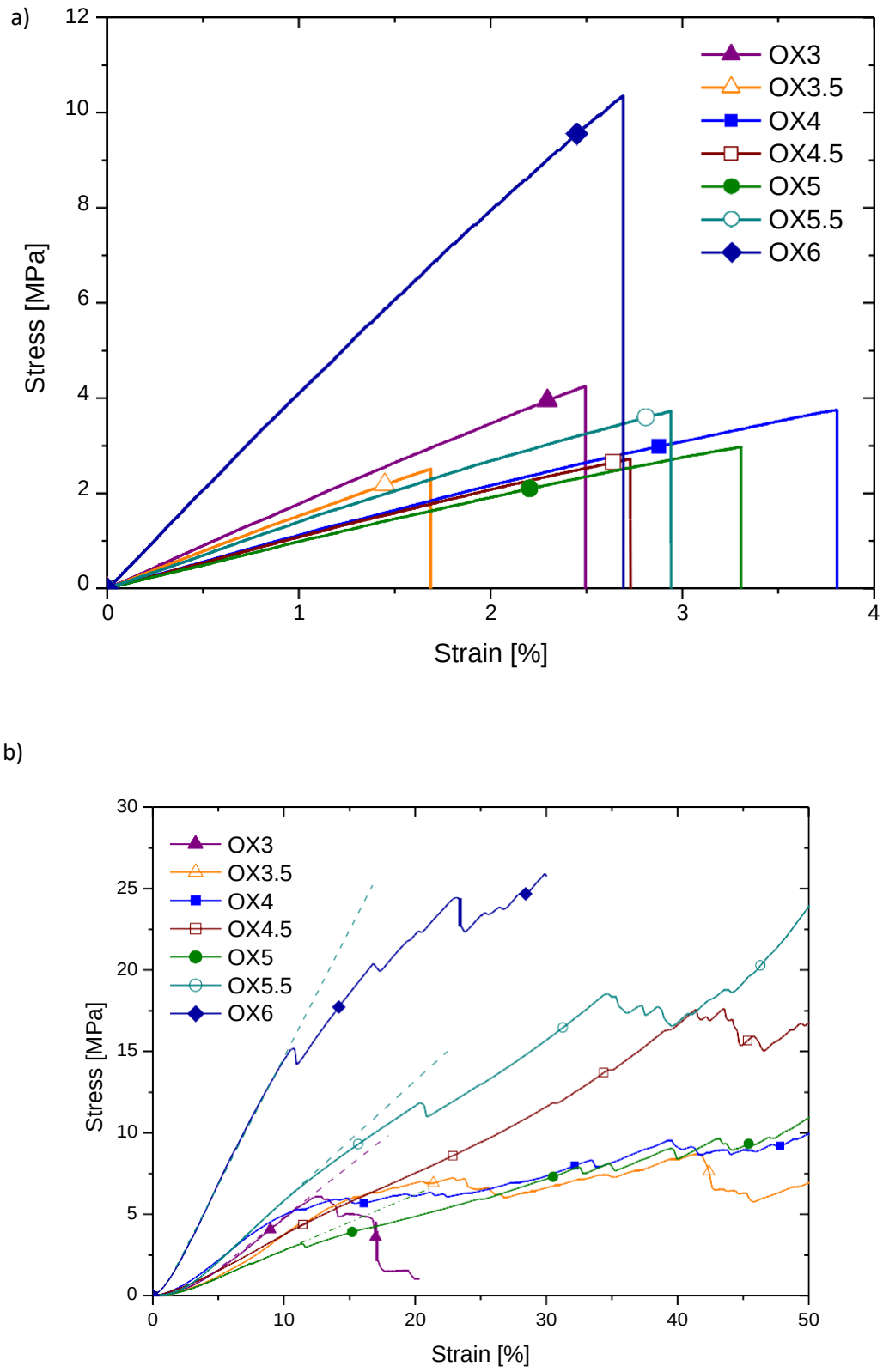

Figure 5. Stress-strain curves for the studied RF xerogel monoliths, under: a) Flexural tests, and b) Compressive tests.

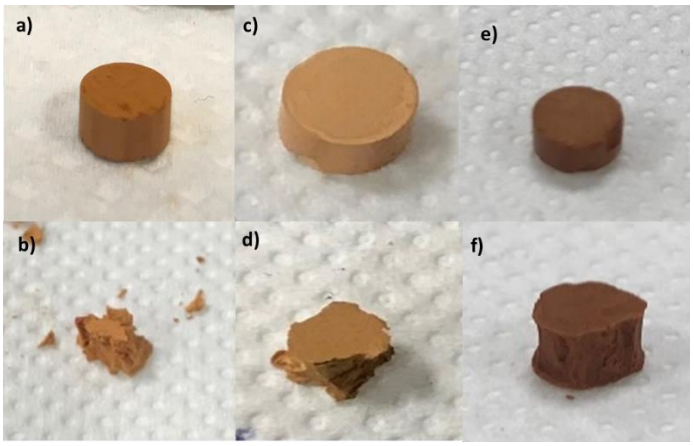

Figure 6. Monolithic RF samples before a) OX3, c) OX4 and e) OX6), and after b) OX3, d) OX4 and f) OX6) compression tests. Photos of the broken monoltihs have been taken at b) 21%, d) 50% and f) 31% strain.

The compression behaviour of the OX3 samples was essentially linear elastic until the yield strength was reached (Figure 5b). Further compression of the monolith quickly led to its failure, which corresponded to the complete bursting of the cylindrical sample (also seen in Figure 6b). On the other hand, the compression tests of the OX6 samples were also characterised by a linear elastic region that, in this case, ended abruptly due to the ejection of small pieces from the monolith (at about 10% strain in Figure 5b). Only in the case of OX6, the stress recovered almost immediately until the next ejection, and so on. Therefore, the high stiffness of this sample is evident when compared to the rest of the xerogels. In addition to withstanding the highest "stress" values, this sample relatively retained its original shape, compared to the rest of OXs after the compression tests (see Figures 6e and 6f). For these two samples, the compressive moduli were calculated from the slope of the initial elastic region and the yield strengths were considered at the end of the same elastic region. The results are collected in Table 2. It should be remarked here that the bursting process characteristic of this type of test compromises the definition of "stress" from the initial cross-section, which changes over the course of the experiment due to the ejection of parts of the monoliths. In any case, only the points of the deformation curves (Figure 5b) recorded well before the

change in the cross-section of the rods were taken into account for the calculation of both compressive modulus and yield strength of the OXs samples reported in Table 2.

Table 2. Mechanical properties of the RF xerogels monoliths.

Sample	C ompressive modulus MPa (STDV)	Compressive (yield) streng th MPa (STDV)	Flexural modulus MPa (STDV)	Flexural strength MPa (STDV)
OX3	66 (5.7)	5.7 (0.7)	174 (7.3)	5.9 (1.4)
OX3.5	54 (7.3)	4.7 (1.1)	152 (9.9)	4.2 (0.8)
OX4	46 (10)	4.0 (1.6)	140 (2.1)	3.8 (0.1)
OX4.5	40 (8.2)	4.5 (0.4)	122 (8.3)	2.7 (0.2)
OX5	37 (7.2)	4.2 (1.6)	124 (3.2)	2.3 (0.4)
OX5.5	70 (9.8)	8.8 (2.1)	130 (7.2)	4.7 (0.9)
OX6	174 (25.4)	19.2 (7.1)	391 (16.7)	10.1(0.6)

The rest of the samples tested fell between the mechanical behaviour of OX3 and OX6. The compression curves included a continuous increase in stress until either a sudden drop happened because of materials' fragmentation or a stress plateau was reached due to elastic-plastic behaviour. These two characteristics appeared combined in most tests of OX3.5-OX5.5 monoliths (Figure 5b). The eventual loss of monolith fragments (Figure 6d) during the compression tests of these materials makes it very difficult to ascribe the stress plateaus to a specific deformation (yield) mechanism. Actually, in some tests (see, for example, the curve of OX5.5 in Figure 5b), there was evidence of a stress recovery after the plateau (at about 35% strain) that suggests either a collapse-densification mechanism of the material microstructure [9,10], or a simple re-accommodation of the beams on the newly exposed surfaces. It should be clear, however, that the stress plateaus of samples OX4.5 and, in particular, OX5 and OX5.5, occurred at higher stress values than those obtained for OX3.5 and OX4. Moreover, the stress recovery after the stress plateau in the latter samples was much more limited or even non-existent. Nevertheless, the compressive moduli and yield strengths were calculated as for samples OX3 and OX6, i.e., the moduli from the slopes of the linear

elastic parts of the stress-strain curves and the strengths as the maximum stresses of the elastic parts (results in Table 2). The trends of the compressive and flexural moduli of the OXs samples (Table 2) are essentially the same. The compressive moduli obtained in this work agree reasonably well with other previously reported values [5,29].

The calculation of the yield strength of the OXs materials is useful to understand better the Hg intrusion profiles in Figure 3. Specifically, it may seem surprising that the samples OX3 and OX3.5 showed a sharp Hg intrusion zone whereas there were two intrusion zones for OX4-OX5.5 (Figures 3 and 4). Bearing in mind the differences in force transmission under isostatic conditions (Hg intrusion) and uniaxial loading (compression tests), it is quite relevant to note that, if the isostatic pressure required to intrude the porous network of the OXs is above their yield strength, an anomalous intrusion profile is registered. Thus, the intrusion of Hg into the porosity of OX3 and OX3.5 is almost complete when the isostatic pressure reaches about 5 MPa (Figure 3), i.e., the yield strength of the two materials (Table 2). This explains the absence of additional bands in their pore size distributions (Figure 4).

The influence of textural properties on the mechanical properties or porous solids has been studied by different authors [9,10,16,30–32]. In general, it seems widely accepted that for a given set of porous materials (e.g. RF organic xerogels), elastic properties are closely related to the density/porosity of the materials, with their stiffness or strength increasing as the density/porosity increases/decreases [9,11]. Figure 7 shows the values of compressive modulus and porosity of the RF xerogels in this study. There is a significant decrease in the porosity values from sample OX5 to OX6, and their compressive moduli increase accordingly. However, the moduli of the OX3-OX4 samples steadily decrease even though their porosity values are essentially the same. The existence of two sets of materials within the OXs series when considering their

mechanical properties in relation to their densities is clearly shown in Figure 8. For both sets of organic xerogels, the selected mechanical properties follow power laws of density.

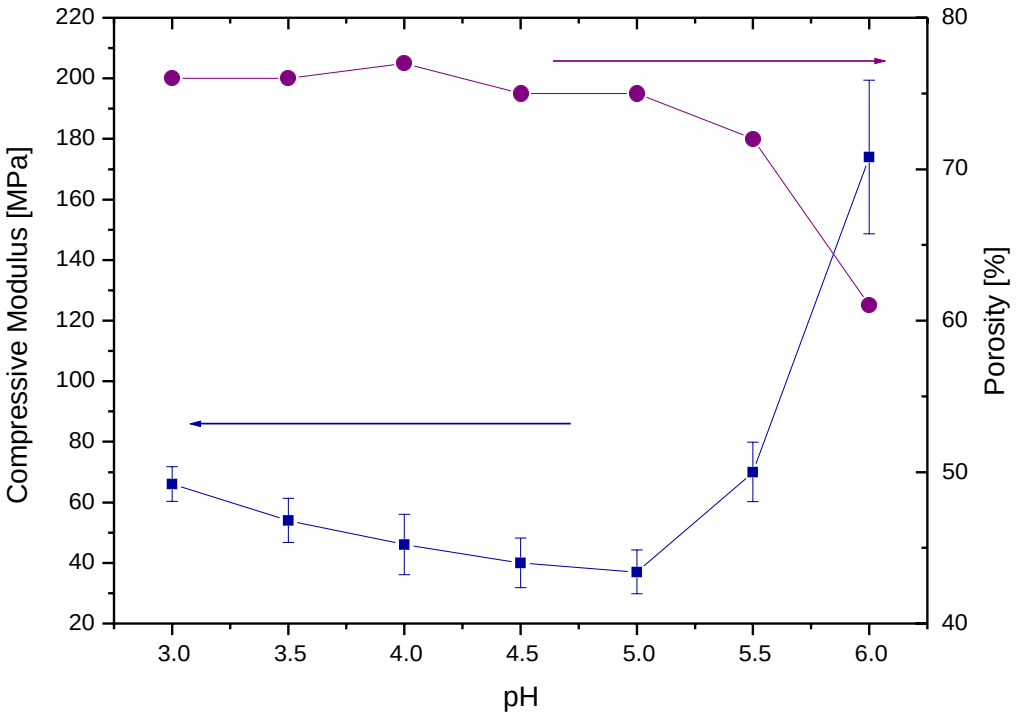

Figure 7. Compressive modulus and porosity of the RF xerogels as a function of the pH of their precursor solutions.

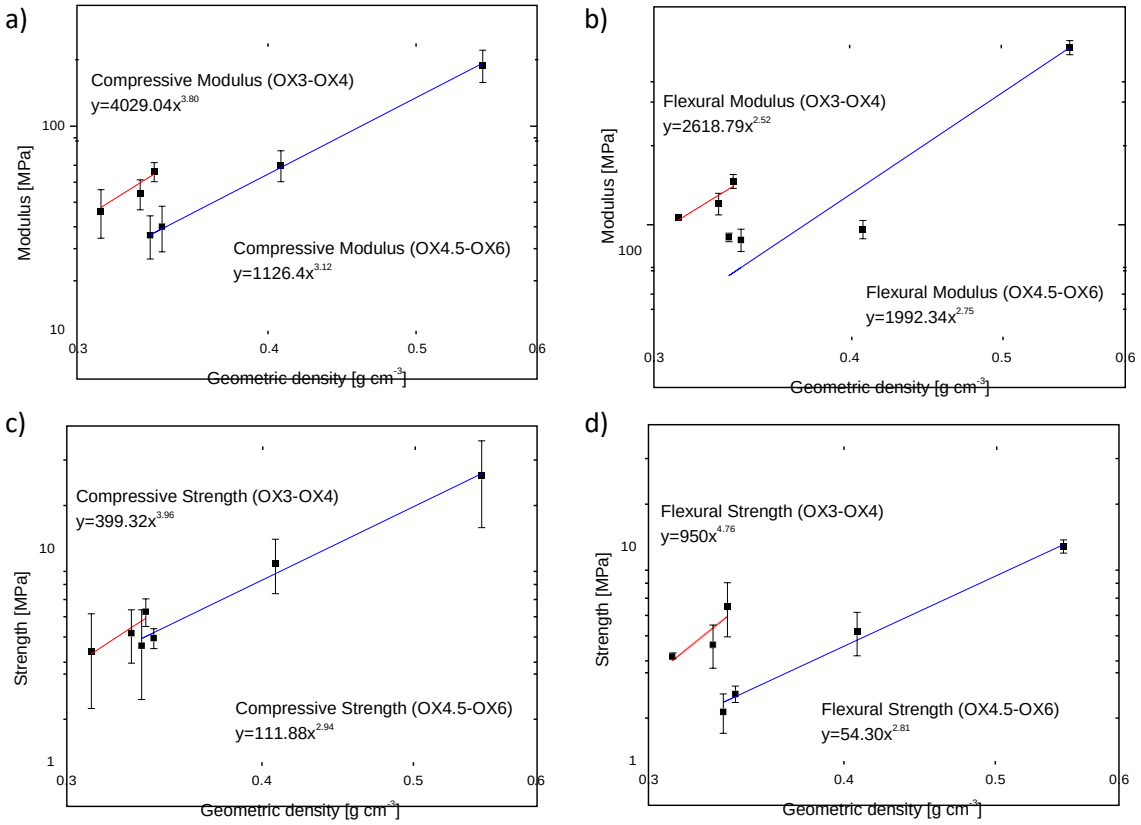

Figure 8. Mechanical properties of RF xerogels as a function of their geometric density, fitted by power laws.

This is not the first time that RF gels of similar porosity/density have shown significant differences in their mechanical properties [19]. The work of Pekala et al. demonstrated that RF aerogels with similar densities have compressive moduli that could differ by one order of magnitude depending on their specific microstructure. For a given density, organic xerogels would then exhibit important differences in their mechanical properties depending on the size of the polymer clusters, which in turn determine their interconnectivity. As a simple rule, Pekala et al. established that the higher the average cluster size, the lower the degree of interconnectivity between clusters, and the lower

the elastic modulus and strength of the RF aerogel [19]. Gross and Scherer theoretically refined this microstructure/mechanical properties relationship in RF gels by introducing the concept of elastic efficiency [18]. They explored the possible effect of non-ideal features of sol-gel materials, such as tortuosity, dispersion in their cluster size and the existence of dangling ends, on their mechanical properties. The latter feature, i.e., the mass of the RF clusters that would contribute to the density of the materials but would be elastically ineffective, was identified as the most important factor that could explain the deviations from the power-law relationship between the mechanical properties and the density of ideal foam-like materials.

In the case of the RF xerogels studied here, the power law exponents for both sets of materials (Figure 8a) are well above 2. However, whereas the exponent of the OX4.5-OX6 set of materials is close to 3, as expected for RF gels [33], that of the OX3-OX4 series is almost 4. Such a high exponent has not been reported before for RF gels, and only silica aerogels exhibit similar values [33, 34]. Moreover, a power-law exponent of 3.8 for the OX3-OX4 series of gels would suggest an extraordinarily low interconnectivity or, in the words of Gross and Scherer [18], a high elastically inefficient mass (many dangling bonds). In the light of this prediction, the relatively high stiffness of OX3 is simply astonishing.

In order to better understand this anomaly, SEM analyses of the samples before and after the compression tests were carried out (Figure 9). It is clearly observed that, as usual, the pH of the precursor solution has a remarkable effect on the size of the polymer clusters. Thus, the higher the pH of synthesis, the lower the cluster size (and pore size) of the resulting material. In OX6 (Figure 9e), small and closely packed polymeric clusters are observed. The porosity of this sample is hardly visible. On the other hand, OX3 (Figure 9a) has big, less connected clusters, thus leaving wide pores

within the xerogel microstructure. Finally, the size of the polymer clusters (and pores) of OX4 (Figure 9c) is lower than that of OX3 but higher than that of OX6.

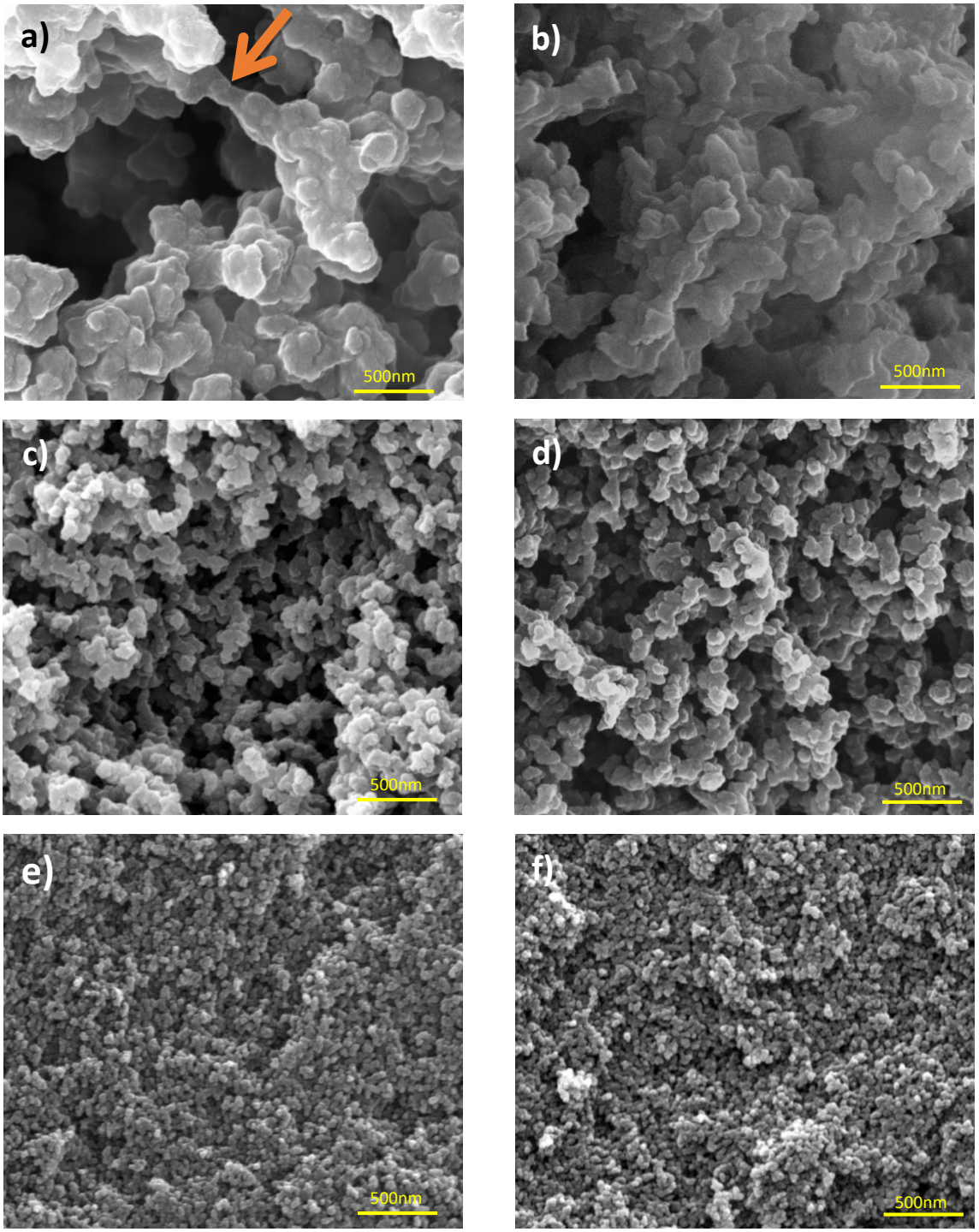

Figure 9. SEM images of xerogels before (a) OX3, c) OX4 and e) OX6) and after (b) OX3, d) OX4 and f) OX6) compression tests. The orange arrow highlights a rod-like microstructure present in sample OX3.

By observing these micrographs, the superior mechanical properties of OX6 could be predicted. In addition, one would expect the stiffness (and maybe the strength) of OX4 to be higher than that of OX3, which is not the case. The key feature that would explain the relatively high stiffness of the latter sample is the presence of elongated microstructures in the OX3 micrographs, as indicated by the orange arrow in Figure 9a. Thus, pillars or struts seem to reinforce the clusters in OX3. The ubiquity of these microstructures in sample OX3 is shown in Figure S4. These rod-like microstructures would bear the compressive load [34], resulting in a stiffer than expected material. The presence of these micro-rods would also help to understand the fracture behaviour of OX3 under compression. Hence, once the micro-rods are broken, the whole system would collapse (burst) since the micro-rods bear far a much higher load than a rod-free microstructure could withstand. In fact, such rod-like microstructures disappear in the OX3 samples observed after the compression test (Figure 9b), which also results in a drastic reduction in the porosity of the sample. In the case of OX4, the deformation mechanism would simply involve the densification of the sample by reorganisation of clusters and reduction of porosity.

4. Conclusions

This work has clearly shown that the mechanical properties of RF xerogels are not only defined by average properties such as density/porosity and cluster size. The synthesis conditions of RF xerogels under acidic pH values result in materials with very high cluster sizes that strongly limit the interconnectivity of the clusters or, more precisely, the elastically effective mass. In this case, however, the acidic environment slows down RF condensation reactions and the pseudo-spherical clusters, which are characteristic of RF xerogels, have time to elongate, giving rise to rod-shaped, potentially denser

microstructures. This completely alters predictions based on previous observations obtained from RF xerogels synthesised using higher contents of basic catalysts. This original finding has not been previously reported to our knowledge, and is a consequence of the wide range of pore sizes and cluster sizes explored here, which allowed us to visualise the effect of these structures.

Acknowledgements

The authors gratefully acknowledge the financial support received from the Consejo Superior de Investigaciones Científicas (Project I-LINK1200), Ministerio de Economía, Industria y Competitividad (Project CTQ2017-87820-R) and Principado de Asturias–FICYT-FEDER (Project PCTI-Asturias IDI/2018/000118). SLFL is grateful to the Administración del Principado de Asturias for her research training grant awarded through the "Severo Ochoa" program. LARM thanks CONACYT, México for a post-doctoral grant (CVU No 330625, 2017).

References

[1] F.M.K. R. W. Pekala, Resorcinol-formaldehyde aerogels and their carbonized derivatives, Polymer Preprints. 30 (1989) 221–223.

[2] N. Job, R. Pirard, J. Marien, J.-P. Pirard, Porous carbon xerogels with texture tailored by pH control during sol–gel process, Carbon. 42 (2004) 619–628. https://doi.org/10.1016/j.carbon.2003.12.072.

[3] G. Hasegawa, T. Shimizu, K. Kanamori, A. Maeno, H. Kaji, K. Nakanishi, Highly Flexible Hybrid Polymer Aerogels and Xerogels Based on Resorcinol-Formaldehyde with Enhanced Elastic Stiffness and Recoverability: Insights into the Origin of Their Mechanical Properties, Chemistry of Materials. 29 (2017) 2122–2134. https://doi.org/10.1021/acs.chemmater.6b04706.

[4] M. Schwan, L. Ratke, Flexibilisation of resorcinol–formaldehyde aerogels, Journal of Materials Chemistry A. 1 (2013) 13462. https://doi.org/10.1039/c3ta13172f.

[5] A. Léonard, S. Blacher, M. Crine, W. Jomaa, Evolution of mechanical properties and final textural properties of resorcinol–formaldehyde xerogels during ambient air drying, Journal of Non-Crystalline Solids. 354 (2008) 831–838. https://doi.org/10.1016/j.jnoncrysol.2007.08.024.

[6] M. Schwan, M. Naikade, D. Raabe, L. Ratke, From hard to rubber-like: mechanical properties of resorcinol–formaldehyde aerogels, Journal of Materials Science. 50 (2015) 5482–5493. https://doi.org/10.1007/s10853-015-9094-x.
[7] N. Rey-Raap, A. Arenillas, J.A. Menéndez, A visual validation of the combined effect of pH and dilution on the porosity of carbon xerogels, Microporous and Mesoporous Materials. 223 (2016) 89–93. https://doi.org/10.1016/j.micromeso.2015.10.044.
[8] N. Job, R. Pirard, J.-P. Pirard, C. Alié, Non Intrusive Mercury Porosimetry: Pyrolysis of Resorcinol-Formaldehyde Xerogels, Particle & Particle Systems Characterization. 23 (2006) 72–81. https://doi.org/10.1002/ppsc.200601011.
[9] M. Letellier, C. Delgado-Sanchez, M. Khelifa, V. Fierro, A. Celzard, Mechanical properties of model vitreous carbon foams, Carbon. 116 (2017) 562–571. https://doi.org/10.1016/j.carbon.2017.02.020.
[10] A. Celzard, W. Zhao, A. Pizzi, V. Fierro, Mechanical properties of tannin-based rigid foams undergoing compression, Materials Science and Engineering: A. 527 (2010) 4438–4446. https://doi.org/10.1016/j.msea.2010.03.091.
[11] J.C.H. Wong, H. Kaymak, S. Brunner, M.M. Koebel, Mechanical properties of monolithic silica aerogels made from polyethoxydisiloxanes, Microporous and Mesoporous Materials. 183 (2014) 23–29. https://doi.org/10.1016/j.micromeso.2013.08.029.
[12] H. Ma, X. Zheng, X. Luo, Y. Yi, F. Yang, Simulation and Analysis of Mechanical Properties of Silica Aerogels: From Rationalization to Prediction, Materials. 11 (2018) 214. https://doi.org/10.3390/ma11020214.
[13] J.S. Noh, J.A. Schwarz, Estimation of the point of zero charge of simple oxides by mass titration, Journal of Colloid and Interface Science. 130 (1989) 157–164. https://doi.org/10.1016/0021-9797(89)90086-6.
[14] M. Thommes, K. Kaneko, A.V. Neimark, J.P. Olivier, F. Rodriguez-Reinoso, J. Rouquerol, K.S.W. Sing, Physisorption of gases, with special reference to the evaluation of surface area and pore size distribution (IUPAC Technical Report), Pure and Applied Chemistry. 87 (2015). https://doi.org/10.1515/pac-2014-1117.
[15] C. Lin, J.A. Ritter, Effect of synthesis pH on the structure of carbon xerogels, Carbon. 35 (1997) 1271–1278. https://doi.org/10.1016/S0008-6223(97)00069-9.
[16] V. Bock, A. Emmerling, J. Fricke, Influence of monomer and catalyst concentration on RF and carbon aerogel structure, Journal of Non-Crystalline Solids. 225 (1998) 69–73. https://doi.org/10.1016/S0022-3093(98)00060-X.
[17] K. Kanamori, R. Ueoka, T. Kakegawa, T. Shimizu, K. Nakanishi, Hybrid silicone aerogels toward unusual flexibility, functionality, and extended applications, Journal of Sol-Gel Science and Technology. (2018). https://doi.org/10.1007/s10971-018-4804-x.
[18] J. Gross, G.W. Scherer, Structural Efficiency and Microstructural Modeling of Wet Gels and Aerogels, Journal of Sol-Gel Science and Technology. 13 (9) 957–960.
[19] R.W. Pekala, C.T. Alviso, J.D. LeMay, Organic aerogels: microstructural dependence of mechanical properties in compression, Journal of Non-Crystalline Solids. 125 (1990) 67–75. https://doi.org/10.1016/0022-3093(90)90324-F.
[20] S. Žalac, N. Kallay, Application of mass titration to the point of zero charge determination, Journal of Colloid and Interface Science. 149 (1992) 233–240. https://doi.org/10.1016/0021-9797(92)90408-E.
[21] ASTM International, ASTM C39 / C39M-18, Standard Test Method for Compressive Strength of Cylindrical Concrete Specimens, ASTM International, West Conshohocken, PA, 2018. https://doi.org/10.1520/C0039_C0039M-18.
[22] ASTM International, ASTM C1684-18, Standard Test Method for Flexural Strength of Advanced Ceramics at Ambient Temperature—Cylindrical Rod Strength, ASTM International, West Conshohocken, PA, 2018. https://doi.org/10.1520/C1684-18.
[23] ASTM International, D790-17, Standard Test Methods for Flexural Properties of Unreinforced and Reinforced Plastics and Electrical Insulating Materials, ASTM International, West Conshohocken, PA, 2017. https://doi.org/10.1520/D0790-17.
[24] G.D. Quinn, The Segmented Cylinder Flexural Strength Test, in: R. Tandon, A. Wereszczak, E. Lara-Curzio (Eds.), Ceramic Engineering and Science Proceedings, John

Wiley & Sons, Inc., Hoboken, NJ, USA, 2006: pp. 295–305. https://doi.org/10.1002/9780470291313.ch28.
[25] G.D. Quinn, R. Morrell, Design Data for Engineering Ceramics: A Review of the Flexure Test, Journal of the American Ceramic Society. 74 (1991) 2037–2066. https://doi.org/10.1111/j.1151-2916.1991.tb08259.x.
[26] J. Kettunen, E.A. Mäkeläa, H. Miettinen, T. Nevalainen, M. Heikkilä, T. Pohjonen, P. Törmälä, P. Rokkanen, Mechanical properties and strength retention of carbon fibre-reinforced liquid crystalline polymer (LCP/CF) composite: An experimental study on rabbits, Biomaterials. 19 (1998) 1219–1228. https://doi.org/10.1016/S0142-9612(98)00027-1.
[27] S.N. White, V.G. Miklus, E.A. McLaren, L.A. Lang, A.A. Caputo, Flexural strength of a layered zirconia and porcelain dental all-ceramic system, The Journal of Prosthetic Dentistry. 94 (2005) 7.
[28] T. Shimizu, K. Kanamori, A. Maeno, H. Kaji, K. Nakanishi, Transparent Ethylene-Bridged Polymethylsiloxane Aerogels and Xerogels with Improved Bending Flexibility, Langmuir. 32 (2016) 13427–13434. https://doi.org/10.1021/acs.langmuir.6b03249.
[29] D.J. Boday, R.J. Stover, B. Muriithi, D.A. Loy, Mechanical properties of hexylene- and phenylene-bridged polysilsesquioxane aerogels and xerogels, Journal of Sol-Gel Science and Technology. 61 (2012) 144–150. https://doi.org/10.1007/s10971-011-2603-8.
[30] T. Woignier, J. Reynes, A. Ha, di Alaoui, I. Beurroies, J. Phalippou, Different kinds of structure in aerogels: relationships with the mechanical properties, Journal of Non-Crystalline Solids. 241 (1998) 45–52.
[31] A. Jain, S. Rogojevic, W.N. Gill, J.L. Plawsky, I. Matthew, M. Tomozawa, E. Simonyi, Effects of processing history on the modulus of silica xerogel films, Journal of Applied Physics. 90 (2001) 5832–5834. https://doi.org/10.1063/1.1412266.
[32] J.D. Lemay, Mechanical Structure-Property Relationships of Microcellular, Low Density Foams., MRS Proceedings. 207 (1990). https://doi.org/10.1557/PROC-207-21.
[33] R.W. Pekalaa, L.W. Hrubesh, T.M. Tillotson, C.T. Alviso, J.F. Poco, J.D. LeMay, A Comparison of Mechanical Properties and Scaling Law Relationships for Silica Aerogels and their Organic Counterparts, MRS Proceedings. 207 (1990). https://doi.org/10.1557/PROC-207-197.
[34] H.-S. Ma, A.P. Roberts, J.-H. Prévost, R. Jullien, G.W. Scherer, Mechanical structure–property relationship of aerogels, Journal of Non-Crystalline Solids. 277 (2000) 127–141. https://doi.org/10.1016/S0022-3093(00)00288-X.

SUPPLEMENTARY INFORMATION

Mechanical properties of resorcinol-formaldehyde xerogels with different porosities

S.L. Flores-López[1], B. Karakashov[2], L.A. Ramírez-Montoya[1], J.A. Menéndez[1], V. Fierro[2], A. Arenillas[1], M.A. Montes-Morán[1,*], A. Celzard[2]

[1]Instituto de Ciencia y Tecnología del Carbono, INCAR-CSIC, Francisco Pintado Fe, 26, 33011, Oviedo, Spain

[2]Institut Jean Lamour, UMR CNRS-Université de Lorraine nº7198, ENSTIB, 27 rue Philippe Séguin, BP 21042, 88051 Epinal cedex 9, France

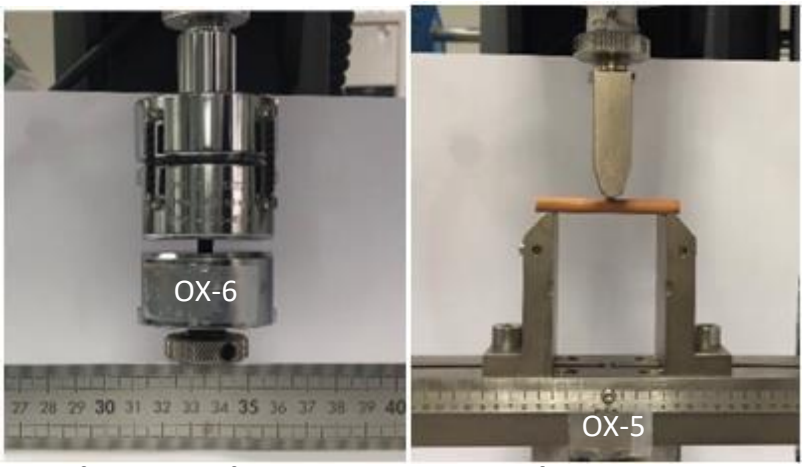

Figure S1. Configuration of INSTRON equipment for uniaxial compression test and three-point flexural test.

Table S1. Elemental analysis of the monolithic RF xerogels.

Sample	Elemental Analysis (wt%, daf)		
	C	H	O
OX3	62.8	4.9	32.3
OX3.5	63.1	4.8	32.1
OX4	66.0	4.5	29.5
OX4.5	63.3	4.8	31.9
OX5	63.7	4.9	31.4
OX5.5	63.6	5.1	31.3
OX6	65.2	4.6	30.2

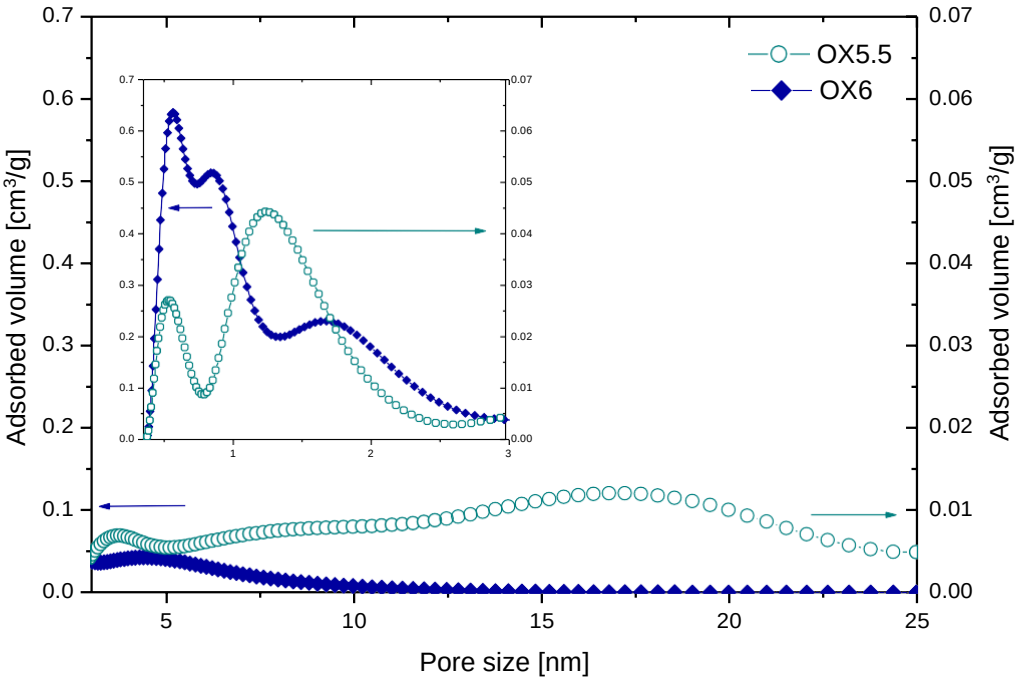

Figure S2. NLDFT pore size distributions calculated from N_2 adsorption isotherms.

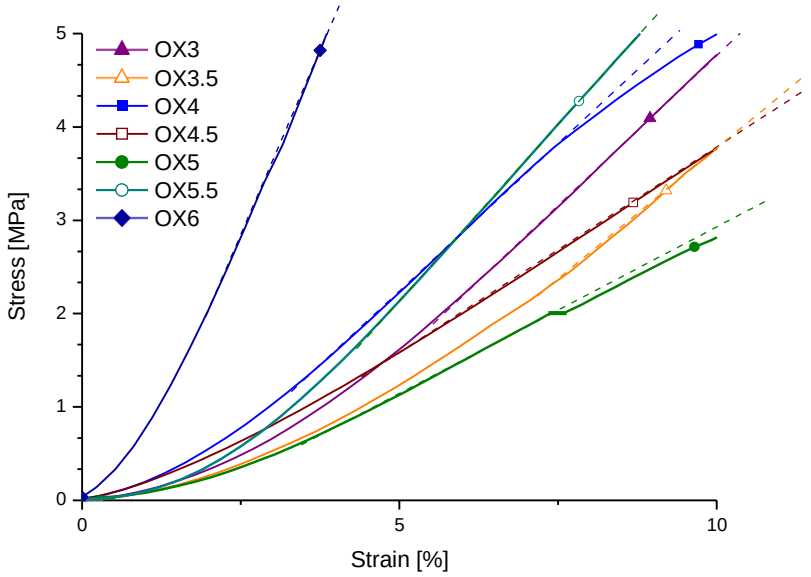

Figure S3. Linear elastic behaviour during the compressive tests of the OXs samples.

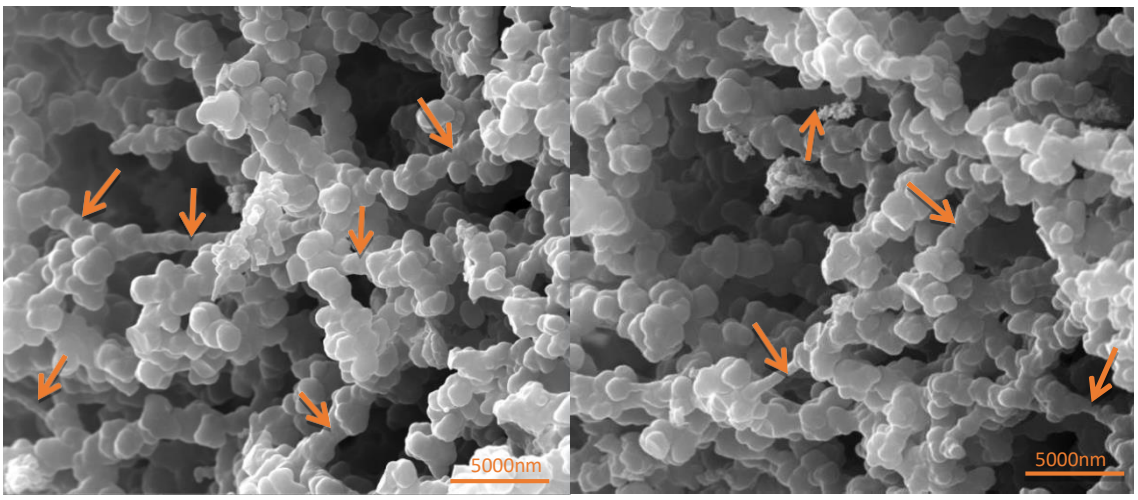

Figure S4. Visualisation of rod-like microstructures (pillars, struts) in sample OX-3.